Design and study of highly negative sensitive mid-infrared surface plasmon resonance sensor based on microstructured fiber for high refractive index sensing

JIAN-FEI LIAO*
School of Mechanical and Electrical Engineering, Wuyi University, Wuyishan 354300, China

A new surface plasmon resonance (SPR) sensor is proposed that uses a microstructured fiber (MF) with a simple structure to detect high refractive index (RI) within the mid-infrared region. Numerical analysis of the sensing properties has been conducted by using a full-vector finite element method, and the simulation findings reveal that the proposed sensor can achieve single-resonance negative RI sensing within the mid-infrared wavelength range of 2.503-2.8 μm when the RI of the analyte varies from 1.50 to 1.52. By optimizing the structure of the sensor, the maximal negative wavelength sensitivity of -15700 nm/RIU and a high amplitude sensitivity of 111 RIU^{-1} are achieved. In addition, the negative RI resolution is as high as -6.37×10^{-6} RIU when the instrument's resolution is 0.1 nm. Therefore, our proposed sensor has a lot of potential for high RI sensing, including the detection of highly active chemical and biological liquid samples.

(Received November 22, 2023; accepted June 3, 2024)

Keywords: Microstructured fiber, Surface plasmon resonance, Refractive index sensor, Mid-infrared

1. Introduction

Surface plasmon resonance (SPR) based sensor is considered a very important advanced detection technology in biomonitoring, environmental monitoring, chemical reaction monitoring, and structural health monitoring due to its high sensitivity to the refractive index (RI) of the analyte [1-3]. Early SPR-based sensors typically require a coupling prism structure, which can be bulky and complex [4,5]. Therefore, prism-based SPR sensors are not suitable for remote sensing and long-range detection applications. Nowadays, optical fiber is employed to remove the bulky prism to solve these defects as it is more flexible and can enhance system integration. The evanescent field leaks to the fiber cladding and attains to the surface of plasmonic materials, and then the SPR effect is generated. To realize high-sensitivity detection, various types of traditional optical fiber-based SPR sensors have been reported [6,7]. For instance, Tubb et al. proposed an SPR sensor based on a tapered single-mode optical fiber [8]. Their experimental findings demonstrated that the index resolution was as high as 5.0×10^{-4} RIU when the RI of the analyte varied from 1.326 to 1.357. To enhance the stability of sensing performance, a SPR sensor was developed by Peng et al. utilizing a multi-mode optical fiber [9]. Thanks to its ability to generate two independent SPR signals, the index resolutions for the polymerized gold SPR and the bare gold SPR channel were as high as 8.889×10^{-5} RIU and 1.0×10^{-4} RIU, respectively. Jiang et al. designed a new type of SPR sensor by employing a U-bent fiber [10]. The experimental results indicated that a high sensitivity of 700.3 nm/refractive index unit (RIU) was realized after altering the sensing range to 1.330-1.3657. A partially uncoated fiber-based SPR sensor was developed by Diez et al. for RI sensing [11]. Their experimental outcomes revealed that the index resolution of the sensor was higher than 1.0×10^{-5} RIU. Furthermore, a highly sensitive SPR sensor was developed by Xi et al. using a D-type optical fiber coated with Au-graphene film [12]. The simulation findings indicated that the highest sensitivity is up to 1223 nm/RIU at the low detection range of 1.3330-1.3657. Nevertheless, the sensitivity of the conditional optical fiber-based SPR sensors is limited to 10^3 nm/RIU due to their fiber structure limitations.

Microstructured fiber (MF), which has periodic air holes in the fiber cladding, is a more flexible alternative to traditional optical fibers. It offers a range of unique features such as controllable fiber dispersion [13], single-mode operation without limits [14], a large core mode area [15], etc. Hence, MF-based SPR sensors have gained more attention due to their unique and outstanding capabilities including high detectable sensitivity, real-time measurement, and label-free sensing [16-22]. Currently, many different kinds of MF-based SPR sensors have been developed to realize highly accurate detection. In 2006, Hassani et al. developed the first MF-based SPR sensor with an inside metal coating method [23]. To generate the SPR effect in the proposed sensor, they used a hexagonal solid-core MF with two layers of air holes. Metalized holes were located in the second layer. The simulation findings indicated that a change in analyte RI from 1.33 to 1.34 resulted in a high RI resolution of 10^{-4} RIU. In 2015, a new type of SPR sensor that grounded on a hexagonal MF with two liquid-filled cores was designed by Rifat et al. [24]. The results showed that when the RI range varied from 1.46 to 1.49, the highest amplitude sensitivity and RI resolution were up to 418 RIU^{-1} and 2.40×10^{-5} RIU,

respectively. In 2017, a mid-infrared SPR sensor using a hexagonal MF with a dual-opening channel structure is developed by Liu et al. [25]. It has been discovered that the sensor can operate in the mid-infrared region of 2.55-2.90 μm. Additionally, the highest sensitivity and RI resolution are up to 13000 nm/RIU and 7.69×10^{-6} RIU within the low sensing range of 1.23-1.29. In 2020, Li et al. proposed an SPR sensor utilizing a H-shaped MF [19]. Benefitting from its H-shaped open structure, a high sensitivity of 12600 nm/RIU was achieved within the detection range of 1.33-1.41. In 2021, Yan et al. developed a new type of MF-based SPR sensor with an elliptical detective channel for high RI sensing [26]. The numerical calculations indicated that the highest sensitivity for wavelength was as high as 12719.97 nm/RIU in the sensing range of 1.43-1.49. In 2022, Bing et al. designed an SPR sensor employing a microchannel MF with a D-shaped dual-core structure [27]. The highest sensitivity and RI resolution of y-polarized mode were up to 33600 nm/RIU and 2.97×10^{-6} RIU within the detection range of 1.33-1.44. Nevertheless, the MF-based SPR sensors that can detect the high RI within the mid-infrared region have rarely been developed. Moreover, some SPR sensors based on PCF with an elliptical structure have also been proposed for RI sensing this year. For example, Du et al. proposed a new type of SPR sensor using an elliptical photonic crystal fiber [28]. The highest wavelength sensitivity and amplitude sensitivity were up to 21,000 nm/RIU and 455.45 RIU^{-1} when the analyte RI lay in (1.20, 1.40). Tang et al. proposed an elliptical channel photonic crystal fiber SPR sensor for magnetic sensing [29]. The magnetic field sensitivity, wavelength sensitivity, and amplitude sensitivity are up to o.739 nm/Oe, 12043.8 nm/RIU, and 754.88 RIU^{-1}, respectively.

In this paper, a new SPR sensor based on a circular liquid-core MF with two layers of air holes is developed for high RI sensing within the mid-infrared regime. The impacts of sensor parameters on sensing performance are thoroughly investigated by employing a full-vector finite element method (FEM). The simulation findings indicate that our proposed sensor can operate in the mid-infrared regime of 2.503-2.8 μm. Moreover, a high negative wavelength sensitivity of -15700 nm/RIU with a negative RI resolution as high as -6.37×10^{-6} RIU is achieved in the high RI detection range of 1.50-1.52, and the amplitude sensitivity of the sensor is 111 RIU^{-1}. To the extent of our knowledge, our developed sensor realized the highest negative wavelength sensitivity among the reported MF-based SPR sensing designs.

2. Sensor design

The geometry of the simulation MF-based SPR sensor is displayed in Fig. 1. A circular lattice structure is formed by two layers of air holes with a radius of R1 in our proposed MF cladding. To realize the high negative RI sensing in the mid-infrared region, a liquid core with a radius of R_2 is introduced in the center of MF to control the mode effective RI of the core mode. Moreover, a semicircular analyte channel structure coated with indium tin oxide (ITO) is employed to achieve single-resonance detection. The other sensor parameters are the inner and outer ring air holes pitch h_1, h_2, the radius of the semicircular analyte channel R_3, the ITO layer thickness t, and the spacing between the bottom of the analyte channel and the fiber central H. The analyte RI is n_a. The RI of the background materials can be obtained from the Sellmeier equation as follows [30].

$$n^2(\lambda)=1+\frac{0.6961663\lambda^2}{\lambda^2-(0.0684043)^2}+\frac{0.4079426\lambda^2}{\lambda^2-(0.1162414)^2}+\frac{0.8974794\lambda^2}{\lambda^2-(9.896161)^2} \tag{1}$$

where λ stands for the wavelength. The permittivity of ITO is calculated from the Drude model [31].

$$\varepsilon=\varepsilon_\infty-\omega_p^2/\left(\omega^2+i\omega\Gamma\right) \tag{2}$$

$$\omega_p^2=ne^2/\left(\varepsilon_\infty m^*\right) \tag{3}$$

where ε is the permittivity of ITO, $\varepsilon_\infty=3.9$ is the high frequency permittivity, ω is the angular frequency, ω_p is the plasma frequency, $\Gamma=1.8\times10^{14}\ rad/s$ is the electron scattering rate, $m^*=0.35m_0$, $m_0=9.1\times10^{-31}\ kg$ is the rest mass of electron, $n=1.8\times10^{21}\ cm^{-3}$ is the carrier concentration of ITO, $e=$ electron charge. Our proposed circle lattice MF can be fabricated by utilizing the stack-and-draw technique. Modified chemical vapor deposition (MCVD) preforms with a flat ground on one side can be used to achieve the semicircular analyte channel structure [32]. Finally, we can employ the atomic layer deposition technique to deposit ITO film [33].

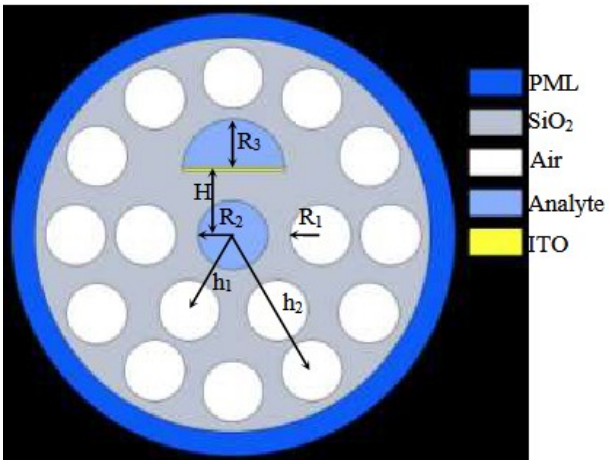

Fig. 1. Schematic of the designed MF-based SPR sensor (color online)

By adopting the full-vector FEM with anisotropic perfectly matched layers, the confinement loss (*CL*) of the

sensor can be obtained utilizing the following formula [31].

$$CL\left(\mathrm{dB}/cm\right)=8.686\times\left(2\pi/\lambda\right)\mathrm{Im}\left(n_{eff}\right)\times10^{4} \quad (4)$$

where λ denotes the operation wavelength of the sensor in vacuum, which has a direct proportional relationship with the imaginary part of the modal effective RI ($\mathrm{Im}(n_{eff})$). The loss of the sensor has a maximum value at the resonance wavelength.

3. Simulation results and discussion

Firstly, the coupling features between the fundamental core mode and surface plasmon polaritons (SPP) mode are studied, and the findings of our numerical analysis are presented in Fig. 2 with R_1=1.9 µm, R_2=2.05 µm, R_3=3.0 µm, H=4.0 µm, h_1=5.3 µm, h_2=9.5 µm, t=90 nm, and n_a=1.52. As indicated in Fig. 2a, the values of Re(n_y) and Re(n_{spp}) gradually reduce when the incident light wavelength changes from 2.38-2.503 µm. But the value of Re(n_{spp}) decreases more rapidly than that of Re(n_y). Additionally, Re(n_{spp}) has a larger value than Re(n_y) between the wavelengths of 2.38-2.503 µm. At the resonance wavelength of 2.503 µm, Re(n_y) is equivalent to Re(n_{spp}). It indicates that the phase-matching resonance condition between these two modes is satisfied. On the other hand, after the resonance point, the value of Re(n_x) enlarges abruptly while the value of Re(n_{spp}) suddenly reduces. This is because the phase of these two modes is affected severely when the SPR effect happens. The resonance characteristics between the y-polarized fundamental mode and SPP mode can also be learned from the insets in Fig. 2(a). To illustrate, a small amount of the E-field energy at the wavelengths 2.42 µm and 2.64 µm is transmitted from the y-polarized fundamental mode to the SPP mode since these two modes state in a weak-coupling situation. But at the coupling resonance wavelength of 2.503 µm, a significant portion of the E-field energy of the y-polarized fundamental mode is coupled into the SPP mode. Similar coupling phenomena can be observed from the loss curves of these two modes, which are given in Fig. 2(b). The loss peak of the y-polarized mode appears at the resonance wavelength of 2.503 µm because of the SPR effect. However, the loss of the x-polarized fundamental mode is minimal and stays almost unchanged throughout the entire wavelength range of 2.38-2.68 m. This is because the interaction strength between the x-polarized and SPP modes is very weak. Hence, this work only focuses on the coupling features between the y-polarized fundamental mode and the SPP mode.

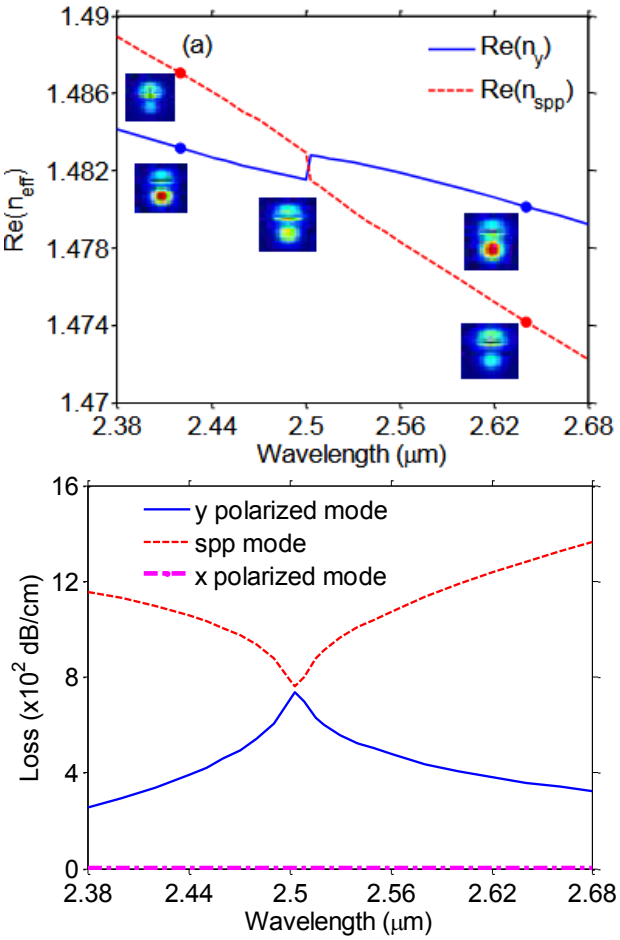

Fig. 2. (a) Dispersion curves of the designed MF-based SPR sensor; (b) Loss spectra of the designed MF-based SPR sensor. Insets are the E-field distributions of two resonance modes (color online)

Fig. 3 depicts the loss properties of the y-polarized mode at different n_a values with R_1=1.9 µm, R_2=2.05 µm, R_3=3.0 µm, H=4.0 µm, h_1=5.3 µm, h_2=9.5 µm, and t=90 nm. Unlike traditional MF-based SPR sensors, the resonant wavelength of our proposed sensor varies towards a shorter wavelength when the value of n_a changes from 1.50 to 1.52, which results in a negative RI sensitivity. This is because a larger n_a leads to a larger Re(n_{spp}), which means the value of the modal effective RI at the resonance point also increases. Then the resonance wavelength of the proposed sensor shifts towards the shorter wavelength range. Peak losses of the y-polarized mode as shown in Fig. 3 are 683 dB/cm, 714.3 dB/cm, and 739.2 dB/cm at the resonant wavelengths of 2.8 µm, 2.643 µm, and 2.503 µm for n_a increasing from 1.50 to 1.52. The reason why peak loss goes up with n_a is that as n_a increases, the interaction strength between the y-polarized and SPP modes is enhanced, and more energy transfer from the y-polarized mode to the SPP mode. On the other hand, a lower peak loss means a lesser energy coupling between these two modes, which causes the resonance spectrum to broaden. To evaluate the detection quality of the sensor, the wavelength sensitivity S_λ can be calculated by adopting the subsequent expression [31].

$$S_\lambda\left(nm/RIU\right)=\Delta\lambda_{peak}\left(n_a\right)/\Delta n_a \quad (5)$$

where $\Delta\lambda_{peak}$ indicates the modification of the peak wavelength while Δn_a is the variation of n_a. The computational result indicate that the high negative wavelength sensitivities of -15700 and -14000 nm/RIU are obtained when n_a changes from 1.50-1.51 and 1.51-1.52, correspondingly. Therefore, the designed sensor offers the highest negative RI resolution of -6.37×10^{-6} RIU when the instrument's resolution is 0.1 nm.

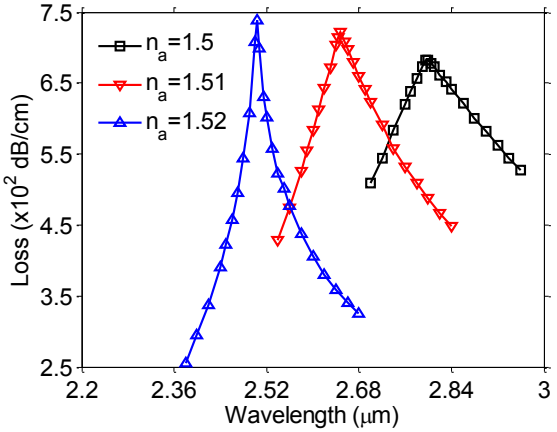

Fig. 3. Loss spectra of the y-polarized fundamental mode at n_a=1.50, 1.51, and 1.52 (color online)

Considering that the sensing ability can be significantly affected by the parameters t, R_2, and R_3, we study the impacts of these three parameters on the resonance wavelength, and the numerical findings are presented in Fig. 4. Fig. 4(a) displays loss spectra of the y-polarized fundamental mode response for n_a=1.52 due to the effect of t with R_1=1.9 μm, R_2=2.05 μm, R_3=3.0 μm, H=4.0 μm, h_1=5.3 μm, and h_2=9.5 μm. As the thickness of the ITO film increases from 90, 95, 100, 105, and 110 nm, the peak loss of the proposed sensor reduces from 739.2, 619.8, 560.2, 526.4 and 505.1 dB/cm occurring at 2.503, 2.513, 2.524, 2.539 and 2.55 μm. The reason is that as t increases, the difficulty of the y-polarized fundamental mode penetrating the surface of the ITO film is improved, which results in less energy transfer from the y-polarized mode to the SPP mode, and then the maximum loss of the y-polarized mode reduces. Similarly, the influence of R_2 on the loss spectra is illustrated in Fig. 4(b) with R_1=1.9 μm, R_3=3.0 μm, H=4.0 μm, h_1=5.3 μm, h_2=9.5 μm and t=90 nm. As R_2 varies from 1.95 to 2.05 μm, the maximum loss of the y-polarized mode reduces from 807.9 to 739.2 dB/cm while the resonance wavelength reduces from 2.609 to 2.503 μm. It is due to the interaction strength between the y-polarized and SPP modes becomes weaker when the value of R_2 increases. As shown in Fig. 4(c) with R_1=1.9 μm, R_2=2.05 μm, H=4.0 μm, h_1=5.3 μm, h_2=9.5 μm, and t=90, R_3 has an opposite effect on the loss spectra to that of t and R_2. When the radius of the semicircular analyte channel enlarges, enhancement affects are introduced, which leads to a larger loss peak and a shift toward longer wavelengths at the resonance point.

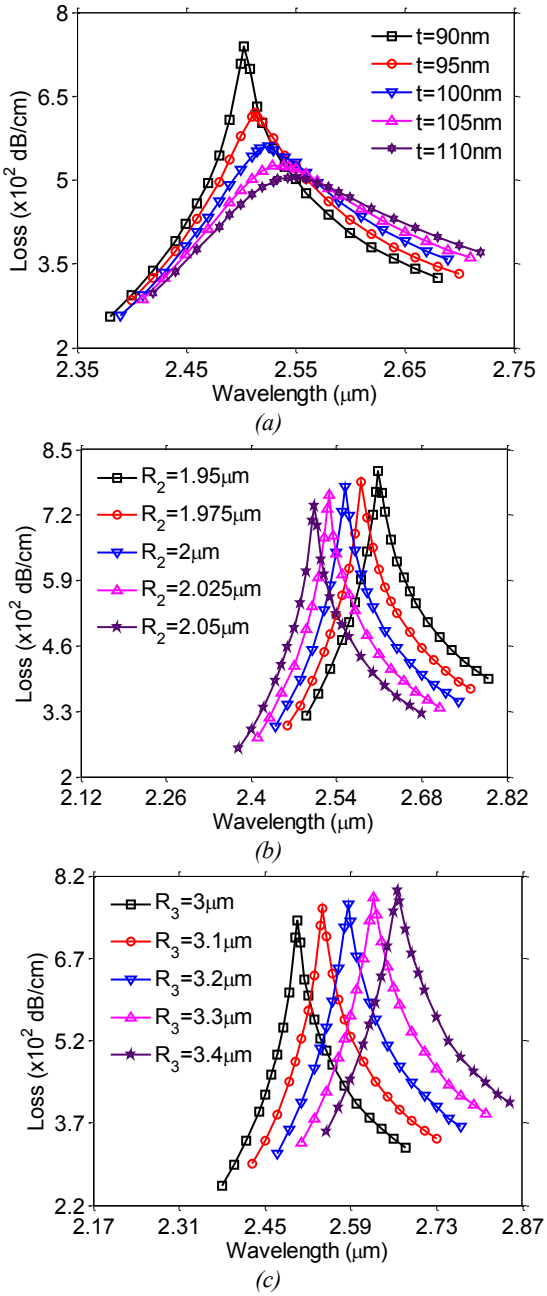

Fig. 4. (a) Effect of sensor parameter t on the loss spectra at n_a=1.52; (b) Effect of sensor parameter R_2 on the loss spectra at n_a=1.52; (c) Effect of sensor parameter R_3 on the loss spectra at n_a=1.52 (color online)

As a crucial factor in evaluating the detection quality, amplitude sensitivity can be calculated by adopting the following expression [31].

$$S_a=-\left(\Delta CL/\Delta n_a\right)/CL_{initial} \quad (6)$$

where ΔCL denotes the loss variation while $CL_{initial}$ stands for the loss in the original state. By adopting equation 3, the effects of the parameters t, R_2, and R_3 on S_a can be simulated, and the numerical outcomes are shown in Fig. 5 with n_a changing from 1.51 to 1.52. Setting the parameters to R_1=1.9 µm, R_2=2.05 µm, R_3=3.0 µm, H=4.0 µm, h_1=5.3 µm, and h_2=9.5 µm, it is evident from Fig. 5(a) that as the value of t increases from 90, 95, 100, 105, and 110 nm, the highest S_a reduces from 111, 67.49, 50.3, 42.01, and 37.02 RIU^{-1}, correspondingly. On the contrary, R_2 has an opposite impact on S_a to that of t, and the simulation outcomes are depicted in Fig. 5(b) with R_1=1.9 µm, R_3=3.0 µm, H=4.0 µm, h_1=5.3 µm, h_2=9.5 µm, and t=90 nm. Such as when R_2 adjusts from 1.95 to 2.05 µm, the maximum S_a increases from 95.54 to 111 RIU^{-1}, and the peak wavelength reduces from 2.609 to 2.503 µm. The reason is that the coupling strength between the y-polarized and SPP modes decreases with R_2 increasing, resulting in a lower $CL_{initial}$, which is verified by the loss spectra shown in Fig. 4(b). Fig. 5(c) displays the influence of R_3 on S_a with R_1=1.9 µm, R_2=2.05 µm, H=4.0 µm, h_1=5.3 µm, h_2=9.5 µm, and t=90. One can learn that R_3 has a similar effect on S_a to that of t. As R_3 changes from 3 to 3.4 µm, the amplitude sensitivity of our proposed sensor decreases from 111 to 76.43 RIU^{-1} due to the loss in the original state $CL_{initial}$ increases with R_3 increasing.

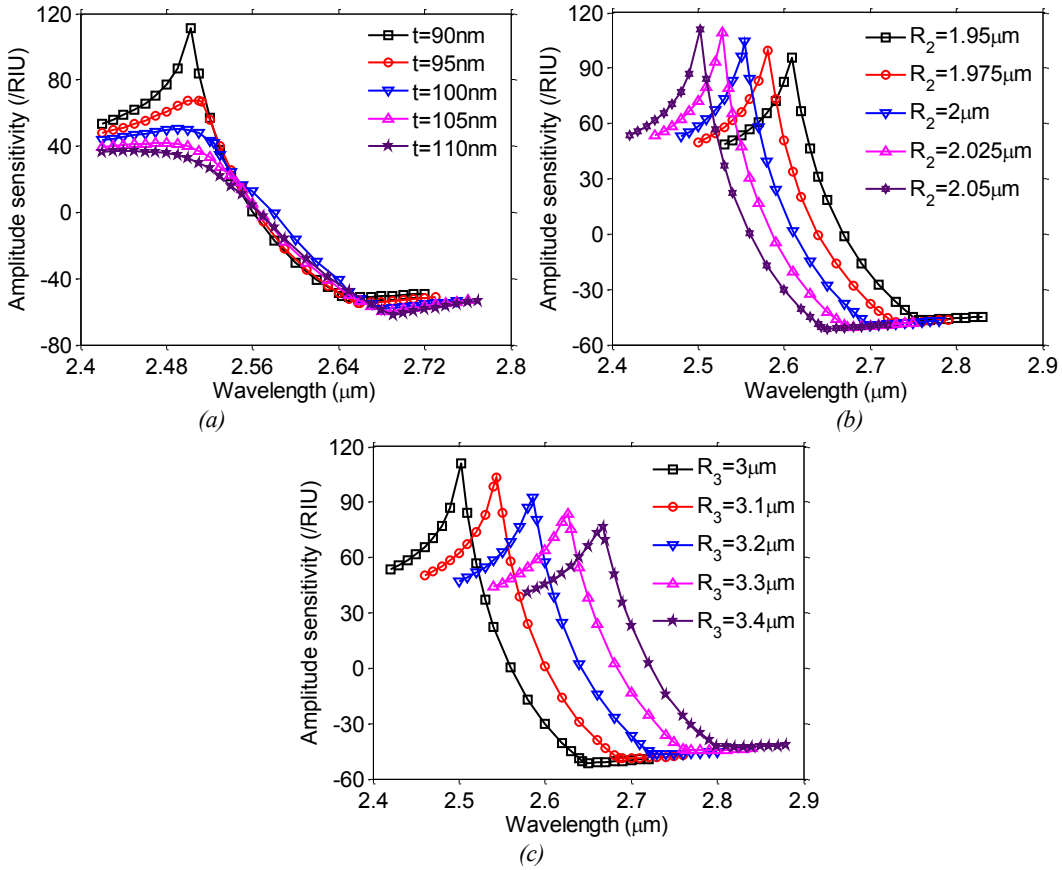

Fig. 5. (a) Effect of sensor parameter t on the amplitude sensitivity with n_a varying of 1.51-1.52; (b) Effect of sensor parameter R_2 on the amplitude sensitivity with n_a varying of 1.51-1.52; (c) Effect of sensor parameter R_3 on the amplitude sensitivity with n_a varying of 1.51-1.52 (color online)

Fig. 6 depicts the affects of the parameters t, R_2, and R_3 on the wavelength sensitivity S_λ with n_a varying from 1.51 to 1.52. According to Fig. 6(a) with R_1=1.9 µm, R_2=2.05 µm, R_3=3.0 µm, H=4.0 µm, h_1=5.3 µm, and h_2=9.5 µm, high negative wavelength sensitivities of -14000, -14500, -14700, -14200, and -14100 nm/RIU are achieved when t changes from 90, 95, 100, 105, and 110 nm. Similarly, the affect of R_2 on S_λ is given in Fig. 6(b) with R_1=1.9 µm, R_3=3.0 µm, H=4.0 µm, h_1=5.3 µm, h_2=9.5 µm and t=90 nm. It is evident that the maximum negative wavelength sensitivity of -14800 nm/RIU occurs at R_2=1.95 µm while the minimum negative wavelength sensitivity of -14000 nm/RIU happens at R_2=2.05 µm. Setting the parameters to R_1=1.9 µm, R_2=2.05 µm, H=4.0 µm, h_1=5.3 µm, h_2=9.5 µm, and t=90, Fig. 6(c) presents the variation in wavelength sensitivity at the radius of the semicircular analyte channel R_3 3, 3.1, 3.2, 3.3, and 3.4 µm. One can find that S_λ increases with the increasing R_3

of 3.1-3.4, and the highest negative S_λ of -14200 nm/RIU is achieved at R_3=3.1 μm. The main reason is that the coupling strength between the y-polarized and SPP modes is enhanced as R_3 increases from 3.1 to 3.4, which results in an improvement in the wavelength sensitivity.

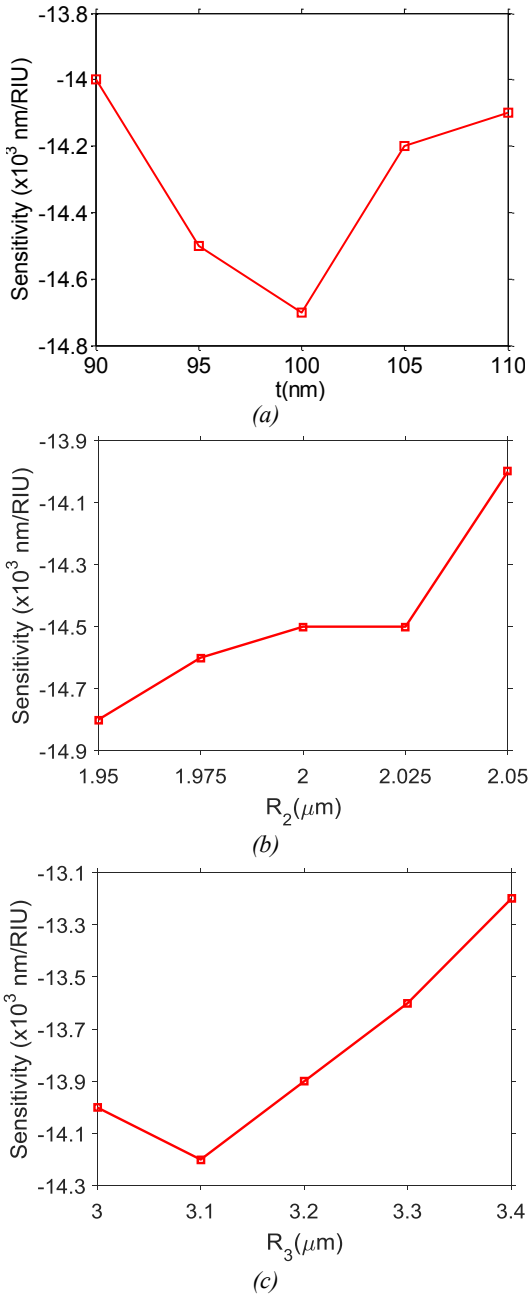

Fig. 6. (a) Effect of sensor parameter t on the wavelength sensitivity with n_a varying of 1.51-1.52; (b) Effect of sensor parameter R_2 on the wavelength sensitivity with n_a varying of 1.51-1.52; (c) Effect of sensor parameter R_3 on the wavelength sensitivity with n_a varying of 1.51-1.52 (color online)

4. Conclusion

A high-sensitivity SPR sensor based on a single analyte-filled core MF is designed for high-RI sensing within the mid-infrared region. To generate the SPR effect in the proposed sensor, ITO is utilized as a plasmonic material coated on the bottom of the analyte channel. The analyte-filled core fiber structure can effectively control the mode effective RI to realize high-RI sensing, while the single analyte channel design can enable the sensor to achieve single-resonance detection within the mid-infrared range of 2.503-2.8 μm. The simulation outcomes indicate that the sensor parameters can effectively affect the sensing performance. Moreover, The highest S_λ and resolution are as high as -15700 nm/RIU and -6.37×10^{-6} RIU, which are much higher than that of these negative sensitive MF-based SPR sensors [34,35]. These findings provide a reference for high-RI detection within the mid-infrared region.

Acknowledgements

This research was funded by the Natural Science Foundation of Fujian Province of China (2022J011193), the Science and Technology Program of Nanping of China (N2021J001) and the Scientific Research Foundation for the Wuyi University (YJ202104).

References

[1] S. K. Mishra, D. Kumari, B. D. Gupta, Sens. Actuators B Chem. **171**, 976 (2012).
[2] Y. Zhao, M. Lei, S. Liu, Q. Zhao, Sens. Actuators B Chem. **261**, 226 (2018).
[3] J. Homola, Chem. Rev. **108**(2), 462 (2008).
[4] W. W. Lam, L. H. Chu, C. L. Wong, Y. T. Zhang, Sens. Actuators B Chem. **105**(2), 138 (2005).
[5] E. Klantsataya, P. Jia, H. Ebendorff-Heidepriem, T. M. Monro, A. Francois, Sensors **17**(12), 12 (2016).
[6] A. K. Pander, A. K. Sharma, C. Marques, Materials **13**(7), 1623 (2020).
[7] A. K. Sharma, B. Kaur, C. Marques, Optik **218**, 164891 (2020).
[8] A. J. C. Tubb, F. P. Payne, R. B. Millington, C. R. Lowe, Sens. Actuators B Chem. **41**(1-3), 71 (1997).
[9] W. Peng, S. Banerji, Y. C. Kim, K. S. Booksh, Opt. Lett. **30**(22), 2988 (2005).
[10] S. Jiang, Z. Li, C. Zhang, S. Gao, Z. Li, H. Qiu, C. Li, C. Yang, M. Liu, Y. J. Liu, Phys. D Appl. Phys. **50**, 165105 (2017).
[11] A. Diez, M. V. Andres, J. L. Cruz, Sens. Actuators B Chem. **73**(2-3), 95 (2001).
[12] X. Xi, J. Xu, S. Li, J. Song, W. Yang, Y. Sun, S. Jiang, Y. Han, X. Fan, Sensors, **20**(4), 991 (2016).
[13] J. Liao, J. Sun, M. Du, Y. Qin, IEEE Photon. Technol. Lett. **26**(4), 380 (2014).
[14] T. Birks, J. Knight, P. Russell, Opt. Lett. **22**(13), 961 (1997).
[15] J. Knight, T. Birks, R. Cregan, P. St. J. Russell, J. Sandro, Electron. Lett. **34**(13), 1347 (1998).

[16] C. Liu, W. Su, F. Wang, X. Li, Q. Liu, H. Mu, T. Sun, P. K. Chu, Technol. Lett. **30**(16), 1471 (2018).
[17] J. Liao, Z. Ding, Y. Xie, X. Wang, Z. Zeng, T. Huang, Opt. Fiber Technol. **60**, 102316 (2018).
[18] E. Haque, M. A. Hossain, F. Ahmed, Y. Namihira, IEEE Sens. J. **18**(20), 8278 (2018).
[19] T. Li, L. Zhu, X. Yang, X. Lou, L. Yu, Sensors **20**(3), 741 (2020).
[20] S. Chakma; M. A. Khalek; B. K. Paul, K. Ahmed, M. R. Hasan, A. N. Bahar, Sensing and Bio-Sensing Research **18**, 7 (2018).
[21] G. An, P. Jia, T. Liang, Y. Hong, H. Wang, A. Ghaffar, J. Xiong, Plasmonics, **15**, 1471 (2020).
[22] X. Ji, N. Luan, W. Zhang, Y. Qi, M. Luo, J. Liu, IEEE Photonics J. **14**(6), 6859006 (2022).
[23] A. Hassani, M. Skorobogatiy, Opt. Express **14**(24), 11616 (2006).
[24] A. A. Rifat, G. A. Mahdiraji, D. M. Chow, Y. G. Shee, R. Ahmed, F. R. M. Adikan, Sensors, **15**(5), 11499 (2015).
[25] C. Liu, L. Yang, X. Lu, Q. Liu, F. Wang, J. Lv, T. Sun, H. Mu, P. K. Chu, Opt. Express, **25**(13), 14227 (2017).
[26] X. Yan, Y. Wang, T. Cheng, S. Li, Micromachines **12**(4), 408 (2021).
[27] P. Bing, Q. Liu, G. Wu, S. Yuan, Z. Li, H. Du, J. Yao, Plasmonics **17**(4), 1471 (2022).
[28] Z. Du, H. Liu, Indian J. Phys, **98**(3), 349 (2024).
[29] H. Tang, F. Sun, T. Shen, Y. Feng, C. Liu, X. Liu, C. Wang, J. Opt. Soc. Am. B, **41**, 998 (2024).
[30] Q. Zhao, J. Liu, H. Yang, H. Liu, G. Zeng, B. Huang, Micromachines **13**(6), 826 (2022).
[31] T. Huang, Plasmonics **12**, 583 (2017).
[32] L. Li, G. Wylangowski, D. N. Payne, R. Birch, Electron. Lett. **19**(22), 1020 (1986).
[33] M. Al. Mahfuz, Md. A. Hossain, E. Haque, N. H. Hai, Y. Namihira, F. Ahmed, IEEE Sens. J. **20**(14), 7692 (2020).
[34] B. Shuai, L. Xia, D. Liu, Opt. Express **20**(23), 25858 (2012).
[35] W. Qin, S. Li, Y. Yao, X. Xin, J. Xue, Opt. Laser. Eng. **58**, 1 (2014).

*Corresponding author: jfliao@126.com